Materials Research Express

PAPER • **OPEN ACCESS**

Anomalous magnetic and electrical properties of disordered double perovskite alloy $LaCaMnFeO_6$

To cite this article: T A Tran *et al* 2024 *Mater. Res. Express* **11** 076101

Materials Research Express

PAPER

Anomalous magnetic and electrical properties of disordered double perovskite alloy $LaCaMnFeO_6$

T A Tran[1], T P Hoang[2,3,*], D T Khan[4,*], A V Rutkauskas[5], S E Kichanov[5], N Q Tuan[4], L V Truong-Son[4], N T Dang[2,3], T L Phan[6], T T Trang[7], A S Abiyev[5,8], S H Jabarov[9], A S Sklyarova[10], E V Bolotov[11] and V S Zakhvalinskii[11,*]

[1] Ho Chi Minh City University of Technology and Education, Ho Chi Minh 700000, Vietnam
[2] Institute of Research and Development, Duy Tan University, Danang 550000, Vietnam
[3] Faculty of Natural Sciences, Duy Tan University, Danang 550000, Vietnam
[4] The University of Danang - University of Science and Education, Danang 550000, Vietnam
[5] Frank Laboratory of Neutron Physics, Joint Institute for Nuclear Research, Dubna 141980, Russia
[6] Faculty of Engineering Physics and Nanotechnology, VNU University of Engineering and Technology, 144 Xuan Thuy, Cau Giay, Hanoi 100000, Vietnam
[7] Institute of Tropical Durability, Joint Vietnam-Russia Tropical Science and Technology Research Center. 63 Nguyen Van Huyen, Cau Giay, Hanoi 100000, Vietnam
[8] Western Caspian University, Baku, AZ-1001, Azerbaijan
[9] Institute of Physics, Ministry of Science and Education Republic of Azerbaijan, Baku, AZ-1143, Azerbaijan
[10] Peter the Great St.Petersburg Polytechnic University, 29 Polytechnicheskaya, St.Petersburg 195251, Russia
[11] Belgorod State National Research University, 85 Pobedy St.; Belgorod 308015, Russia
[*] Authors to whom any correspondence should be addressed.

E-mail: hoangtrongphuc@dtu.edu.vn, dtkhan@ued.udn.vn and zakhvalinskii@bsu.edu.ru

Keywords: magnetism, phase transition, crystal structure, double perovskite alloy

OPEN ACCESS

RECEIVED
2 April 2024

REVISED
10 June 2024

ACCEPTED FOR PUBLICATION
3 July 2024

PUBLISHED
12 July 2024

Abstract

Double perovskite alloys are of significant interest owing to their intriguing magnetic properties and potential practical applications. In this study, we provided a detailed report on the structural, electrical and magnetic features of the double perovskite $LaCaMnFeO_6$, prepared via the conventional solid-state reaction technique. Neutron diffraction analysis showed that the sample is single-phase adopting the *Pnma* orthorhombic structure with random distribution of La^{3+}/Ca^{2+} and Mn^{4+}/Fe^{3+} ions on A- and B-sites, respectively. A long-range G-type antiferromagnetic order was formed below $T_N = 250$ K. Magnetic measurements unveiled a cluster glassy behavior at low temperatures with a complex distribution of cluster magnetic anisotropy energy. Ferromagnetic clusters consisting of two Mn^{4+} and one Fe^{3+} were found to exist in the paramagnetic phase. The complex magnetic properties of $LaCaMnFeO_6$ are attributed to the cation disorder effect combined with the competition between magnetic interactions. Unusual electrical behavior with a large positive magnetoresistive effect was observed and correlated to magnetic phase transitions.

1. Introduction

Double perovskite (DP) alloys, represented as $A_2BB'O_6$ (A represents alkaline or rare earth ions, B and B' stand for transition metal ions) have attracted great attention due to their compelling properties like substantial magnetodielectric coupling, colossal magnetoresistance, giant dielectric constant, magnetocaloric effects, spin-driven ferroelectricity, giant exchange bias, and spin-phonon coupling [1–4]. The physical properties of DP materials are highly sentitive to the cation ordering degree over octahedral sites, influenced by the differences in charge and ionic size between the B and B′ elements.

In perfectly ordered DPs, where the difference in charge state and radii of B and B′ ions is essential, B and B′ cations alternate at the octahedral sites with the B–O–B′ superexchange interaction exerting a dominant role on their magnetic properties. Conversely, the similarity in charge states or ionic radii of *B* and *B′* leads to the cation-disorder within the DPs [5]. In the disordered phase, the chemical and/or structural disorder gives rise to the

coexistence of multiple competing superexchange interactions between B and B′ spins leading to multiphase behavior with diverse magnetic transitions, spin frustration, Griffiths phase, spin-glass, and exchange bias effect [5–8].

Among the DP materials, La_2MnNiO_6 and La_2MnCoO_6 have become subjects of intense research due to the observation of near room-temperature ferromagnetism (FM) [8–10]. La_2MnNiO_6 exhibites FM with the Curie temperature near room temperature [11]. It has been reported that the presence of the disordered phase in La_2MnNiO_6 sharply reduced the Curie temperature [12]. A similar behavior has been found in La_2MnCoO_6 [13]. The decrease of T_C in the cationically disordered La_2MnCoO_6 was attributed to the introduction of Co–O–Co and Mn–O–Mn bonds into the matrix of Mn–O–Co bonds in the ideally ordered La_2MnCoO_6, weakening the overall FM in the La_2MnCoO_6 [14].

Interestingly, despite structural similarities with La_2MnNiO_6 and La_2MnCoO_6, the magnetic properties of La_2MnFeO_6 present a more complex and intriguing scenario, marked by discrepancies among reports in both theoretical and experimental researches. Qian *et al*, using density-functional calculations, predicted FM behavior in La_2MnFeO_6, arising from the coupling between neighboring high-spin-state Fe^{3+} ions and intermediate-spin-state Mn^{3+} ions [15]. In contrast, Ndiaye *et al,* using GGA + U calculations, proposed a ferrimagnetic (FiM) ground state for La_2MnFeO_6 due to local electron–electron interactions in the Fe-*d* orbital favoring the Fe^{3+} valence state over Fe^{2+} one [8]. Moreover, Yoshimatsu *et al* experimentally reported the FiM behavior in La_2MnFeO_6 thin films with antiferromagnetic (AFM) coupling between Mn^{3+} and Fe^{3+} ions [16]. Furthermore, Barrozo *et al* observed a formation of FM clusters below 150 K and a long-range FM phase below 75 K in La_2MnFeO_6 bulk samples synthesized by the combustion method [17]. Palakkal *et al* observed a Griffiths-like transition at 425 K and spin-glass-like transition at 60 K in disordered polycrystalline La_2MnFeO_6 synthesized by the Pechini method [18]. Interestingly, these magnetic transitions occurred at higher temperatures in La_2MnFeO_6 nanoparticles prepared through the ionic coordination reaction method [18]. The diverse observations underscore the critical role of synthesis methods in the magnetic properties of La_2MnFeO_6 DP.

Furthermore, recent researches have shown the effect of ion substitutions at both A-site and/or B-site on the physical properties of La_2MnFeO_6 DP [19–21]. These substitutions typically induce distortions in the crystal structure, modify the charge state of Fe and Mn ions, and, consequently, alter the balance between magnetic interactions within the materials [19]. Notably, Brahiti *et al* observed a significant enhancement in the Curie temperature T_C of La_2MnFeO_6 induced by the substitution of Ba for La [21]. Furthermore, GGA + U calculation of Ndiaye *et al* revealed a trend of $LaAMnFeO_6$ (A = Ba, Sr, Ca) to exhibit T_C close to the room temperature, making them promising for practical applications in room-temperature magnetic refrigeration [20]. In this work, we have gained insight into the impact of the substitution of Ca for La on the magnetic and electrical properties of $LaCaFeMnO_6$. This investigation aims to further our understanding on the role of ion substitutions in tailoring the properties of DP materials with potential implications for their use in various applications.

2. Experimental details

The $LaCaMnFeO_6$ (LCMFO) compound was prepared using the solid-state reaction technique from starting oxides La_2O_3, $CaCO_3$, Mn_2O_3, and Fe_2O_3 mixed in stoichiometric proportions. The mixture was heated in air at 1320 °C in successive steps for 15, 5, and 15 h. The final heating took place for 22 h at 1375 °C. Intermediate materials were finely reground between each heating stage.

Experiments on neutron powder diffraction (NPD) were carried out on the DN-12 diffractometer at the IBR-2 (JINR, Russia) high-flux pulsed reactor [22]. Data were measured over the temperature range of 10–300 K, with a data collection time of 2 h per temperature point. The scattering angle was 90° and the spectral resolution was $\Delta d/d = 0.015$. The data refinement was perfomed using the Fullprof package with the Rietveld method.

The magnetic characteristics of LCMFO were examined using a superconducting quantum interference device (SQUID). The temperature dependence of magnetization $M(T)$ was measured in both zero-field-cooled (ZFC) and field-cooled (FC) regimes under different applied magnetic fields ranging from 20 to 1000 Oe with the temperature step of 2 K. Thermoremanent magnetization (TRM) curves were measured after cooling sample from the ambient temperature down to 4 K under the same magnetic fields used for the ZFC/FC experiments and the fields were turned off. Following a 100 s waiting period, data were collected upon warming the sample at the rate of 1 K min^{-1}. Hysteresis loops and virgin magnetization curves were measured at selected temperatures in the fields up to 10 kOe. The valence of Fe ion was determined using ^{57}Fe Mössbauer spectroscopic spectra. The spectra were collected in a transmission geometry with the maximal Doppler velocity of 10.00 mm s^{-1}, employing a 25- mCi Co57/Rh gamma source. The temperature dependence of electrical resistivity was investigated within the temperature interval of 10–350 K using the six-probe method. The temperature control

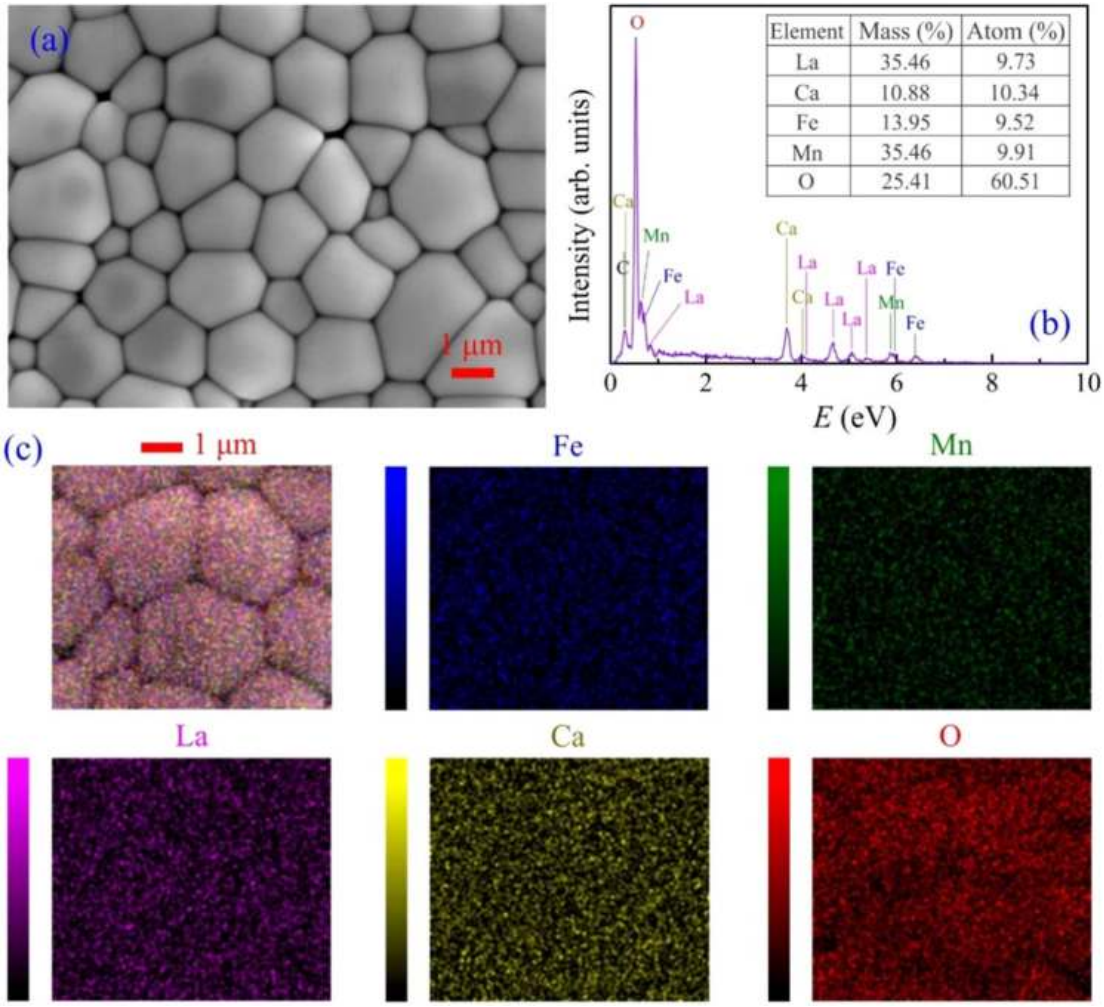

Figure 1. (a) SEM image showing the micro-sizes particles, (b) EDS spectrum, and (c) EDS mappings of a selected region in the compound. The inset shows the atomic percentage of elements of La, Ca, Fe, Mn, and O in the compound.

was facilitated by a closed-cycle helium refrigerator (JANIS CCS-350S) with the temperature determination accuracy of 0.5%.

3. Results and discussion

Figure 1(a) shows a SEM image of the LCMFO compound. The compound mainly consists of large hexagonally and heptagonally shaped particles with the average size of ~2.1 μm interspersed with smaller sized particles of ~1.2 μm. These micro-sized particles exhibit smooth surfaces and clear boundaries. Figures 1(b) and (c) show the EDS analysis of the compound. As can be seen in the inset of figure 1(b), the atomic ratio of elements La:Ca:Mn:Fe:O is almost 1:1:1:1:6 consistent with the chemical formula of $LaCaMnFeO_6$. The EDS result demonstrates the purity of synthesized material. Furthermore, the EDS mappings of a selected region on the sample surface (figure 1(c)) demonstrate the uniform distribution of elements in the compound.

The structural and magnetic characteristics of LCMFO were examined by the NPD method at temperatures ranging from 300 K to 10 K. Figure 2(a) shows the NPD patterns of the synthesized sample collected at selected temperatures. The data refinement showed that the sample is single-phase, crystallizing in a disordered *Pnma* orthorhombic structure (figure 2(b)), in which La/Ca and Fe/Mn randomly distribute at their possible crystallographic sites. The crystal structure remains unchanged across the entire studied temperature range (see table 1). Notably, the oxygen concentration was attempted to be refined during the refinement of the room-temperature NPD patterns, which contains only pure nuclear diffraction peaks. We found that the refinement of the oxygen concentration did not lead to a remarkably better fit between calculated and experimental data and the refined oxygen concentration is 3.02(4), implying the stoichiometry of the studied sample. Furthermore, using the charge neutrality constraint along with considering the pure 3+ valence of Fe ions, shown below by Mössbauer results, and the oxygen stoichiometry of the LCMFO sample, it can be inferred that the sample

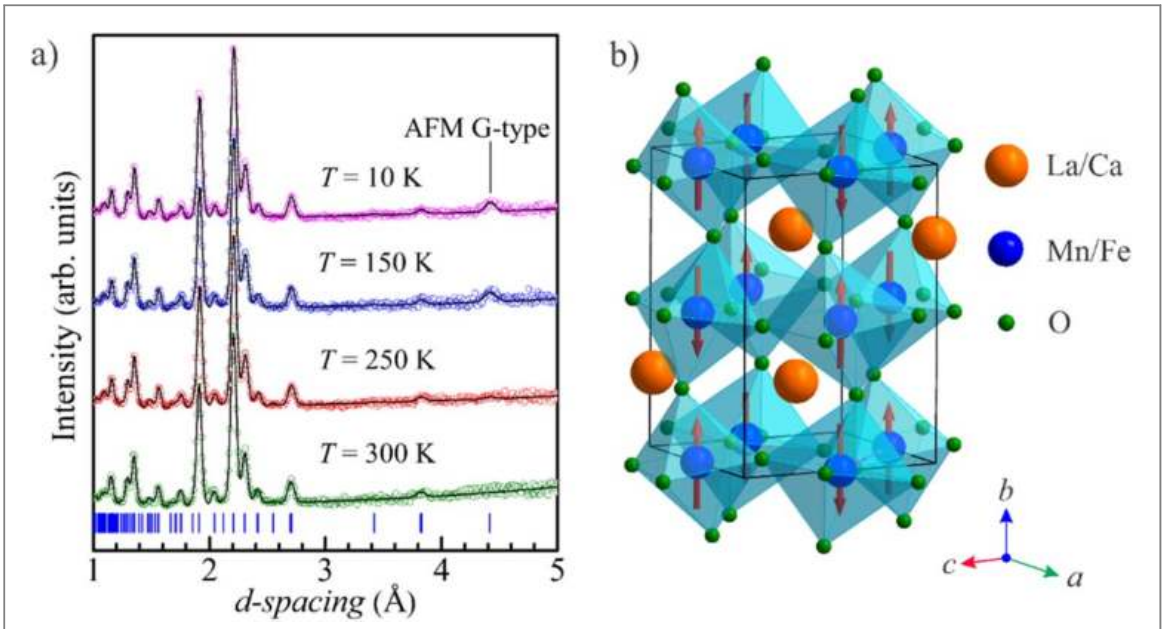

Figure 2. (a) NPD patterns of LCFMO, collected at selected temperatures, are shown along with the fitting curves obtained using the Rietveld method. The positions of the structural peaks are indicated by bottom vertical ticks. The characteristic peak of the AFM G-type phase is denoted as 'AFM G-type'. (b) The illustration of the *Pnma* orthorhombic crystal structure and spin arrangement in the G-type AFM order of LCFMO.

Table 1. Structural details of LCFMO refined from the Rietveld analysis of the NPD data. Atomic positions in the *Pnma* structure are La/Ca *4c* (x, 1/4, z), Mn/Fe *4b* (0, 0, 1/2), O1 *4c* (x, 1/4, z), and O2 *8d* (x, y, z).

T(K)	10	50	150	200	250
a(Å)	5.418(4)	5.419(4)	5.419(4)	5.419(4)	5.417(4)
b(Å)	7.680(6)	7.682(7)	7.679(7)	7.680(7)	7.687(7)
c(Å)	5.422(5)	5.420(5)	5.424(6)	5.425(6)	5.420(6)
La/Ca: x	0.022(2)	0.023(2)	0.020(3)	0.018(3)	0.020(2)
z	−0.008(4)	−0.007(4)	−0.007(5)	−0.006(5)	−0.005(4)
O1 : x	−0.007(3)	−0.005(3)	−0.006(4)	−0.005(4)	−0.005(3)
z	0.427(3)	0.426(3)	0.426(3)	0.427(3)	0.427(2)
O2: x	0.276(3)	0.275(3)	0.275(2)	0.275(2)	0.276(3)
y	0.030(1)	0.029(1)	0.029(2)	0.029(3)	0.028(1)
z	0.719(3)	0.717(3)	0.719(3)	0.718(3)	0.719(3)
Mn/Fe–O1	1.961(4)	1.962(4)	1.962(4)	1.961(4)	1.962(3)
⟨Mn/Fe–O2⟩	1.942(11)	1.942(16)	1.941(19)	1.942(14)	1.940(16)
Mn/Fe–O1–Mn/Fe	156.60(2)	156.35(2)	156.31(2)	156.64(2)	156.68(2)
Mn/Fe–O2–Mn/Fe	161.2(9)	161.3(9)	161.7(9)	161.6(8)	161.8(9)
μ_{AFM} (μ_B)	0.84(6)	0.82(5)	0.71(5)	0.63(6)	—
R_p (%)	2.68	2.68	2.92	2.89	2.51
R_{wp}(%)	3.42	3.38	3.73	3.80	3.27
R_e (%)	2.37	2.37	3.36	3.36	2.80

contains almost only Mn^{4+} ions. This result is consistent with findings in a previous report employing x-ray absorption spectroscopy and neutron techniques [23].

Below $T_N = 250$ K, a magnetic contribution to the intensity of the structural reflection (011) at $d_{hkl} = 4.41$ Å appears and continuously increases upon further decreasing the temperature. The data analysis showed that this peak corresponds to the formation of a long-range AFM G-type phase, in which each pair of nearest neighbor spins are antiparallel, as shown in figure 2(b). It should be noticed that there is not any FM contribution to the intensity of the structural reflections (101)/(020) at $d_{hkl} = 3.83$ Å, indicating the absence of any FM component of the AFM phase or a long-range FM phase. Figure 3 depicts the temperature-dependent evolution of the average magnetic moment $\mu_{AFM}(T)$ and its fitting curve by the emperical function [24]: $\mu_{AFM}(T) = \mu_{AFM0}(1-T/T_N)^{\beta}$, where μ_{AFM0} is the average magnetic moment in the AFM phase at $T = 0$ K, T_N is the Neel magnetic ordering temperature, and β is a fitting parameter. The fitted value of T_N and μ_{AFM0} are 250(2) K and

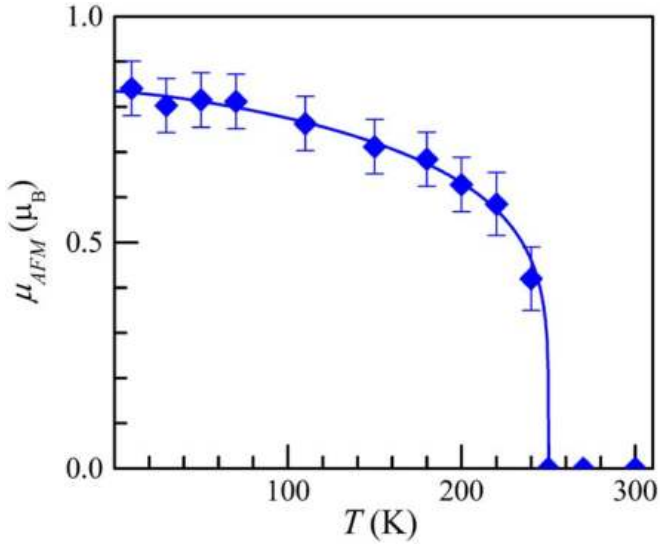

Figure 3. Average magnetic moment of the AFM G-type phase as a fucntion of temperature.

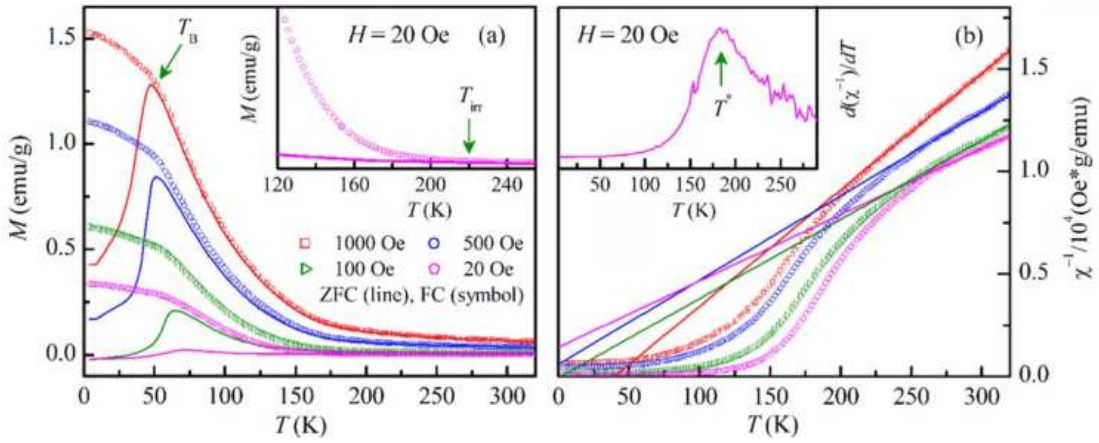

Figure 4. Temperature dependence of (a) ZFC and FC magnetizations and (b) inverse FC susceptibility (χ^{-1}) of LCMFO at various applied magnetic fields H. The insets show (a) a zoom view in the temperature range from 120 to 260 K for the M(T) curve at $H = 20$ Oe and (b) temperature dependence of $d(\chi^{-1})/dT$ at $H = 20$ Oe.

0.86(3) μ_B, respectively. The obtained value of T_N in this study is close to that observed for the G-type AFM order in cation-disordered $BiSrFeMnO_6$ and $BiLaFeMnO_6$ DPs [25]. The value of μ_{AFM0} is much smaller than the average magnetic moment of high-spin-state Fe^{3+} and Mn^{4+} for LCMFO. The fraction of the long-range AFM phase is estimated to be about 3.6%, implying an inhomogeneous magnetic state in the studied sample.

For further insight into the magnetic properties, the temperature-dependent curves of ZFC and FC magnetizations were recored at various magnetic fields of 20, 100, 500, and 1000 Oe (figure 4(a)). It is evident that the ZFC and FC curves coincide and behave paramagnetically at high temperatures. Below a critical temperature T_{irr} (For example, ≈ 220 K at $H = 20$ Oe in the inset of figure 4(a)), the ZFC and FC curves become to diverge, implying a thermally magnetic irreversibility in the sample. The divergence significantly increases with further decreasing temperature and a broad peak is observed in the ZFC curves at T_B (≈62 K at $H = 20$ Oe), indicating the onset of a magnetization blocking process. As increasing the applied field, T_{irr} and T_B shift to lower temperature with a suppression of the divergence in the FC and ZFC magnetizations. It is worth noting that the thermo-magnetic irreversibility along with the peak in the ZFC magnetization are common features for superparamagnetic, cluster-glass-like, spin-glass-like states related to the magnetic anisotropic effect [26, 27]. However, the values of T_{irr} and T_B are often very close in spin-glass states [27, 28], which is not observed in the studied sample ($T_{irr} \gg T_B$). In addition, in spin-glass systems, the FC magnetization is temperature-independent

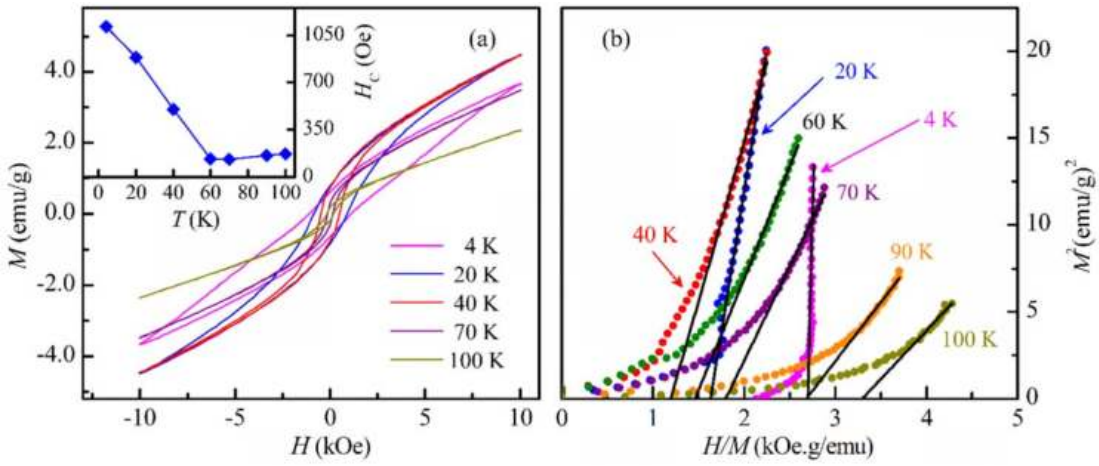

Figure 5. (a) H-dependent magnetization curves $M(H)$ and (b) Arrott plots M^2 versus H/M at selected temperatures under the external magnetic field H up to 10 kOe. The inset shows the temperature dependence of magnetic coercivity H_C.

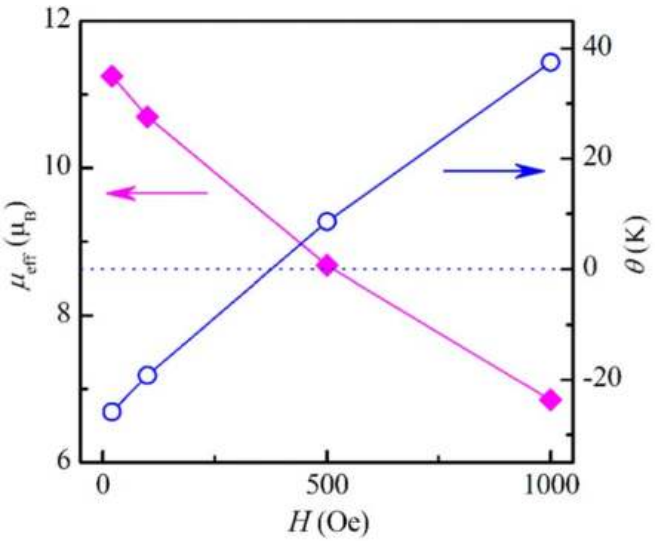

Figure 6. The variation of the Curie–Weiss temperature θ_p and effective paramagnetic moment μ_{eff} of LCMFO with the applied magnetic field.

below T_B, while in our case, the FC curve continuously increases with decreasing the temperature, similar to that usually found in FM cluster glass systems.

Moreover, the remanent magnetization and clear hysteresis loops in the $M(H)$ data (figure 5(a)), which cannot occur in superparamagnetic systems, rule out the possibility of superparamagnetism [27, 28]. On the other hand, the Arrott plots M^2 versus H/M derived from the magnetization isotherms at various temperatures of 4–100 K are demonstrated in figure 5(b). Notably, none of the linear extrapolations at the high field region of the curves yields a positive M^2 intercept, indicating the absence of spontaneous magnetization and short-range nature of FM orders in the whole temperature range. Additionally, the cluster glass state with close T_B and T_{irr} was also observed in La_2MnFeO_6 [29]. Considering these points, it is reasonable to suggest a cluster-glass-like origin of magnetization in the studied sample.

To shed more light on the magnetic interaction, the Curie–Weiss law, $1/\chi = (T - \theta_p)/C$, was employed to fit the paramagnetic region of inverse FC susceptibility curves (figure 4(b)). Here, C is the Curie constant and θ_p is the Curie–Weiss temperature. The effective paramagnetic moment μ_{eff} in Bohr magnetons can be derived using the relation $C = \mu_{eff}^2/3k_B$, in which k_B is the Boltzmann constant. The variation of θ_p and μ_{eff} as a function of the applied field is present in figure 6. It can be seen from figure 6 that θ_p is small negative at low H ($\theta_p = -25.82$ K for $H = 20$ Oe), which monotonously increases and changes its sign at $H \geqslant 380$ Oe. This indicates competing AFM and FM magnetic interactions in the studied sample. Another noteworthy point is the large value of the

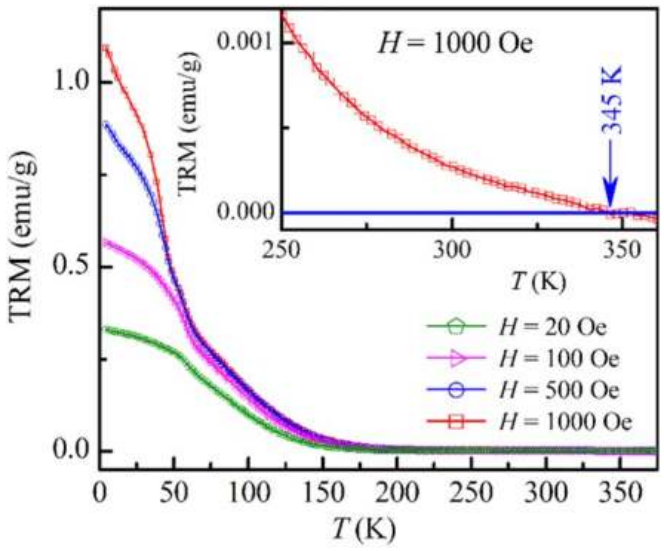

Figure 7. Temperature dependence of TRM at selected magnetic fields. The inset showa a zoom view of the TRM versus T cure at $H = 1000$ Oe demonstrating the onset of FM clusters.

Table 2. Calculated values of S and μ_{eff} for the clusters with different ionic compositions.

Number of spins	Mn^{4+}/Fe^{3+}	S	μ_{eff}
2	0/2	4	8.94
2	1/1	3.5	7.94
2	2/0	3	6.93
3	0/3	6	12.96
3	1/2	5.5	11.95
3	2/1	5	10.95
3	3/0	4.5	9.95

effective moment μ_{eff} which was obtained as 11.2 μ_B at $H = 20$ Oe. The effective Bohr magneton number μ_{eff} for 3d ions is defined as $\mu_{eff} = g\sqrt{S(S+1)}$, where g is the Landé factor and S is the spin angular momentum quantum number [30]. Assuming $g = 2$, $S = 5/2$ for high-spins Fe^{3+} ion and $S = 3/2$ for Mn^{4+} ion, the spin-only value of LCMFO is expected to be 7.94 μ_B smaller than the experimentally obtained one, suggesting the contribution of FM clusters in the paramagnetic matrix. The value of μ_{eff} was calculated for some clusters configurations of Mn^{4+} and Fe^{3+} and displayed in table 2, from which we found that a cluster consisting one Fe^{3+} and two Mn^{4+} ions has the effective moment of 10.95 μ_B which comes closer to the experimental one.

Further, we attempted to propose possible configurations for the FM clusters. The cation disorder leads to the existence of several superexchange paths between Fe^{3+} and Mn^{4+} ions: $Mn^{4+}(d^3)$-O-$Mn^{4+}(d^3)$, $Fe^{3+}(d^5)$-O-$Mn^{4+}(d^3)$, and $Fe^{3+}(d^5)$-O-$Fe^{3+}(d^5)$. According to the Goodenough–Kanamori–Anderson rules [20, 21, 31], the $Fe^{3+}(d^5)$-O-$Fe^{3+}(d^5)$ superexchange is strong AFM, while the $Mn^{4+}(d^3)$-O-$Mn^{4+}(d^3)$ one is weak AFM. This is consistent with the fact that the AFM G-type ordering temperature T_N of isostructural $LaFeO_3$ and $La_{0.60}Sr_{0.40}FeO_{2.8}$ containing only Fe^{3+} ions [32] ($T_N \sim 700$ K) is much larger than $T_N \approx 120$ K of the G-type phase of $CaMnO_3$ containing only Mn^{4+}. The $Fe^{3+}(d^5)$-O-$Mn^{4+}(d^3)$ superexchange is expected to be moderate FM [20, 21, 31]. Moreover, the contribution of double exchange to the FM interaction between Fe^{3+} and Mn^{4+} ions can exist [33]. Therefore, we proposed a plausible model for these three-spin FM clusters, where the Fe^{3+} ion is positioned between two Mn^{4+} ions. The FM interactions within these clusters are likely mediated by exchanges between Fe^{3+} and Mn^{4+} ions through oxygen.

Moreover, figure 7 shows thermoremanent magnetization (TRM) measured at zero magnetic field after cooling from the temperature above magnetic ordering temperatures under selected magnetic fields. By increasing the temperature, the TRMs reduce with a sharp change in the slope around 60 K and approach zero at 345 K, corresponding to a paramagnetic state. The existence of TRM reflects the presence of a FM component and the temperature point 345 K can be considered as the onset temperature of FM clusters. The high value of the onset FM cluster temperature signifies a strong FM interaction within the FM clusters, whereas the

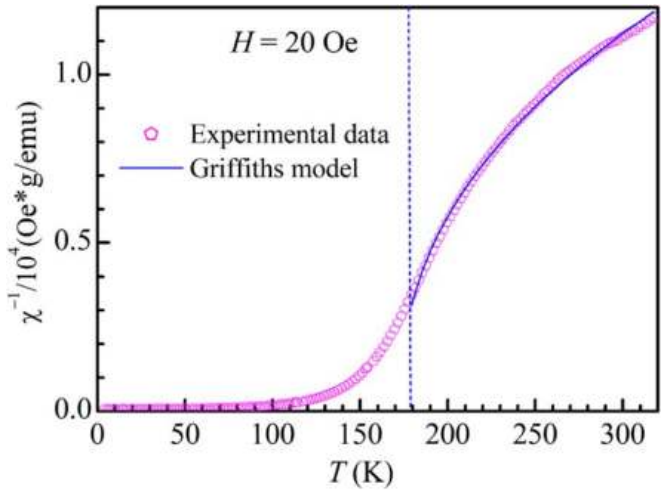

Figure 8. Fitting the inverse FC magnetic susceptility data of LCMFO measured at $H = 20$ Oe using the Griffiths model.

interaction between clusters is rather weak, as indicated by the small value of θ_p. These FM regions begin interacting with each other, resulting in a sharp increase in the magnetization below a specific temperature T^* ($\approx$185 K at $H = 20$ Oe), which can be defined as the position of the maximum in the $d\chi^{-1}/dT$ derivative curve (see the inset in figure 4(b)) [34]. Additionally, μ_{eff} decreases as increasing the magnetic field (figure 6), which can be explained due to an increase in the polarization of spins in the PM matrix overshadowing the contribution from the FM clusters [35–37].

Furthermore, the high-temperature FM clusters in the studied sample exhibit features of a Griffiths phase (GP): a downward divergence from the Curie–Weiss line that gradually softens as the magnetic field increases (figure 4(b)). To clarify the GP nature of these FM clusters, the inverse susceptibility data has been analyzed by using the following equation describing the GP singularity [35–37]: $\chi^{-1} \propto (T - T_C^R)^{1-\lambda}$, where λ lies between 0 and 1 and reflects the strength of the GP, T_C^R defines the GP temperature interval ($T_C^R \leqslant T \leqslant T_G$). T_G is defined as the temperature at which the system is completely paramagnetic. In the case of the studied sampe, T_G is 345 K as defined by the TRM data above. As shown in figure 8, the above-mentioned equation provides a sastifactory fit to the inverse FC magnetic subseptiblity at $H = 20$ Oe with the obtained parameters $T_C^R = 172.9(6)$ K and $\lambda = 0.57(1)$. Notably, the value of λ is comparable with those previously reported for other double perovskites [35, 37], proving the presence of the GP in the LCFMO sample. According to previous works on DPs [26, 36–38], the observed GP in the studied sample can be ascribed to the quenched disorder resulting from the inhomogeneous distribution of Mn and Fe ions giving rise to the complex completion of magnetic interactions.

Furthermore, the valence state of Fe and magnetic properties of LCMFO were also studied using the ^{57}Fe Mössbauer technique. The room-temperature Mössbauer spectrum of the sample, shown in figure 9, exhibits only one typical paramagnetic doublet with the isomer shift δ of 0.344 mm s^{-1} and the quadrupole splitting Δ of 0.398 mm/s. From the obtained values δ and Δ, we can conclude that Fe ions are entirely trivalent and in a high spin state ($S = 5/2$) [39]. At $T = 77$ K, in addition to the paramagnetic doublet, the Mössbauer spectrum exhibits three weak magnetic sextets numbered as (1), (2), and (3) corresponding to the magnetic hyperfine fields of 39.8, 48.2, and 25.3 T, respectively. The presence of these sextets may be attributed to different environments around octahedral Fe^{3+} ions resulting from the random distribution of Mn^{4+} ions [25]. On the other hand, it is anticipated that the magnetic hyperfield at Fe^{3+} ions decreases with an increasing number of nearest-neighbor Mn^{4+} ions [25]. Comparing this Mössbauer result with that obtained for isostructural $BiSrFeMnO_6$ at 80 K [25], which also contains only Fe^{3+} and Mn^{4+} ions, the magnetic hyperfine fields obtained for (2), (1), and (3) sextets correspond to the cases when one Fe^{3+} ion has 0, 1, and 2 nearest-neighbor Mn^{4+} ions, respectively. The relative area of three magnetic sextets is quite close of 15% much smaller compared to that of 55% for the doublet, implying that about half of Fe spins in LCMFO behave paramagnetically even at low temperatures. This observation is in contrast to the complete disappearance of the paramagnetic doublet in $BiSrFeMnO_6$ at 80 K [25], implying a more complex magnetic frustration in the sample under investigation. The observed coexistence of the paramagnetic and magnetic components in the studied system can be attributed due to the nonuniformity of magnetic cluster sizes. The paramagnetic doublet arises from Fe^{3+} spins in small-sized magnetic clusters, where the relaxation time τ is shorter than the Larmor precession time τ_L of the iron nuclear

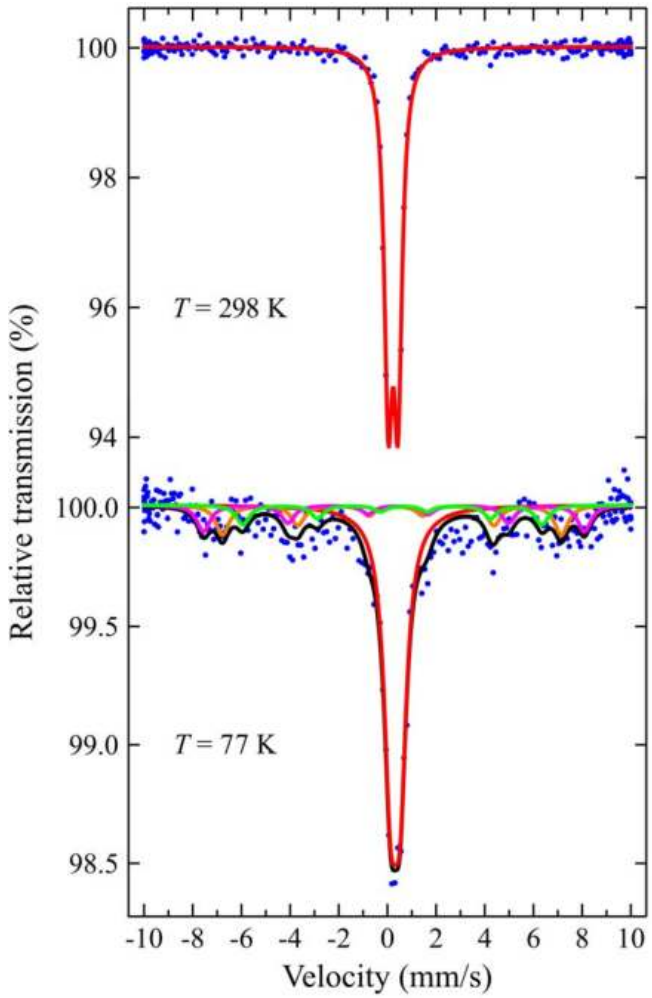

Figure 9. Mössbauer spectra of LCMFO recorded at 298 and 77 K. The black solid line represents the fitted curve, which is the sum of one paramagnetic doublet (red) and the magnetic sextets numbered as (1), (2) and (3).

moment [40]. Conversly, Fe spins within large clusters, characterized by $\tau > \tau_L$, exhibit magnetic hyperfine splitting [40].

Another interesting feature of LCMFO is anomalous transport properties related to the magnetic transitions. Figure 10 demonstrates a semiconducting behavior above T^* and the resistivity data is well fitted by the variable range hopping (VRH) model (see the inset in figure 10(b)): $\rho = \rho_0.\exp(T_0/T)^{1/4}$ [30, 36]. The value of $T_0^{1/4}$ determined from the fit is 167 $K^{1/4}$, which is consistent with those reported for other perovskites exhibiting the quenched disorder [30, 41]. However, below T^*, there is a noticeable change in the resistivity characterized by a sharp decrease in the slope. This signifies the emergence of new conduction channels with heightened electron conductivity. This change can be ascribed to the increased contribution of the electron transport through FM clusters paths within the material [30, 42]. These FM clusters likely facilitate more efficient electron conduction pathways, leading to the observed decrease in the resistivity below T^* [30, 42]. Interestingly, within temperature range of 60–100 K, the sample demonstrates a metal-like conducting behavior, wherein the resistivity decreases as cooling the sample. However, below 60 K, the resistivity becomes less temperature-dependent and exhibits a slight increase with the decrease of temperature. Notably, at this temperature point, we also observed a sharp enhancement in the magnetic coercivity (see the inset in figure 5(a)), indicating this phenomenon relating to the blocking process of FM clusters. Interestingly, under a magnetic field of $H = 1$ T, at temperatures below 60 K, the resistivity sharply increases with a noticeable change in rate around 40 K, whereas it remains almost unchanged in other temperature ranges.

The transport properties of LCMFO can be explained by a scenario proposed for inhomogeneous magnetic systems [42]. The total resistivity of these systems comprises contributions from both FM and non-FM regions. Above T^*, the FM clusters are sparse and exist in isolation, the conduction process is primarily governed by the paramagnetic phase, resulting in the VRH behavior. As temperature decreases, the FM clusters grow in both size and quantity, and below the critical point T^*, the electrical transport becomes dominated by the hopping of

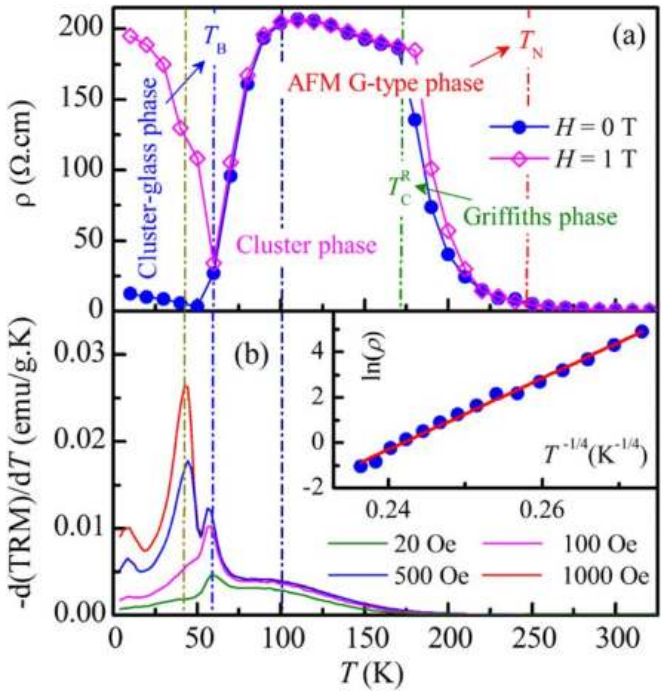

Figure 10. (a) Temperature-dependent resistivity of LCMFO under $H = 0$ and 1 T. (b) The derivative TRM curves with respect to T. The inset shows the fitting of high-temperature data of resistivity based on the VRH model.

electrons between these clusters. Concurrently, the observation of the metallic behavior indicates that the FM clusters are metallic, wherein electrons are delocalized within these regions.

It is worth to noting that the transition points in the resistivity curves coincide with the maxima of the peaks in the derivative of the TRM, dTRM$/dT$ (see figure 10(b)), which can be used as an estimate of the anisotropy energy barrier distribution of clusters E_a [43]. On the other hand, E_a is dependent on several factors including cluster size and shape, surface state, magnetic anisotropy constant of individual cluster and intercluster interaction [43]. As depicted in figure 10(b), there is a broad peak in the dTRM$/dT$ curve at 100 K around the semiconductor–metal-like transition, which is slightly affected by the magnetic field. This evidences that these FM clusters have a broad distribution in size and are responsible for the electrical conduction in LCMFO. In contrast, the lower-temperature peaks in the dTRM$/dT$ curve at 60 and 40 K demonstrate a sharp increase in the intensity under higher magnetic fields. This indicates the H-induced increase in the population of clusters, which is responsible for the positive magnetoresistance in LCMFO. We think that the magnetic nature of these clusters differs from the high-temperature metallic ones. To gain deeper insights into the origin of the positive magnetoresistance in LCMFO, further experimental and theoretical investigations on structural and magnetic properties of clusters under magnetic fields are required.

4. Conclusion

Our investigation has comprehensively examined the complex structural, magnetic and electrical characteristics of the DP LCMFO synthesized by the conventional solid-state reaction method. The analysis has elucidated that the DP LCMFO was disordered and had the *Pnma* orthorhombic crystal structure with a stochastic arrangement of La^{3+}/Ca^{2+} and Mn^{4+}/Fe^{3+} ions on the A- and B-sites, respectively. Notably, the neutron diffraction analysis exposes the emergence of long-range G-type AFM order below $T_N = 250$ K, while magnetic investigations unveil a cluster glassy behavior at lower temperatures, demonstrating a complex distribution of cluster magnetic anisotropy energy. Furthermore, the identification of ferromagnetic clusters, comprising two Mn^{4+} and one Fe^{3+} ion, within the paramagnetic phase underscores the compound's intricate magnetic behavior. These complex magnetic properties were attributed to the disruptive influence of cation disorder and the competitive interplay between magnetic interactions. Moreover, we observed an anomalous electrical behavior, including a significant positive magnetoresistive effect, which is correlated with magnetic phase transitions. Overall, our findings offer valuable insights into the nuanced magnetic and electrical responses of the DP LCMFO, underscoring the importance of its structural intricacies and magnetic interactions in understanding its fundamental properties.

Acknowledgments

The work was supported by the Vietnam Ministry of Education and Training grant No. B2022-SPK-07.

Data availability statement

All data that support the findings of this study are included within the article (and any supplementary files).

ORCID iDs

D T Khan https://orcid.org/0000-0002-7505-8456
T L Phan https://orcid.org/0000-0001-8163-028X
V S Zakhvalinskii https://orcid.org/0000-0001-7055-8243

References

[1] Anand K *et al* 2022 Giant exchange bias in antiferromagnetic $Pr_2CoFe_{0.5}Mn_{0.5}O_6$: a structural and magnetic properties study *J. Phys. D: Appl. Phys.* **55** 365004
[2] Alam M *et al* 2023 Giant dielectric constant, magnetocaloric effect and spin-phonon coupling in $EuTbCoMnO_6$ semiconductor *Physica B: Condens. Matter.* **665** 415043
[3] Saha-Dasgupta T 2020 Double perovskites with 3*d* and 4*d*/5*d* transition metals: compounds with promises *Mater. Res. Express* **7** 014003
[4] Tiittanen T, Vasala S and Karppinen M 2019 Assessment of magnetic properties of $A_2B'B''O_6$ double perovskites by multivariate data analysis techniques *Chem. Commun.* **55** 1722–5
[5] Anand K, Alam M, Pal A, Singh P, Kumari S, Joshi A G, Das A, Mohan A and Chatterjee S 2021 Existence of Griffiths phase and unusual spin dynamics in double perovskite Tb_2CoMnO_6 *J. Magn. Magn. Mater.* **528** 167697
[6] Mohanty P, Marik S and Singh R P 2023 Magnetism and Exchange Bias Properties in Ba_2ScRuO_6 *Magnetochemistry* **9** 144
[7] Sahoo R C, Takeuchi Y, Ohtomo A and Hossain Z 2019 Exchange bias and spin glass states driven by antisite disorder in the double perovskite compound $LaSrCoFeO_6$ *Phys. Rev. B* **100** 214436
[8] Gauvin-Ndiaye C, Baker T E, Karan P, Massé, Balli M, Brahiti N, Eskandari M A, Fournier P, Tremblay A M S and Nourafkan R 2018 Electronic and magnetic properties of the candidate magnetocaloric-material double perovskites La_2MnCoO_6, La_2MnNiO_6, and La_2MnFeO_6 *Phys. Rev. B* **98** 125132
[9] Zhang C, Zhang Y, Nie Z, Wu C, Gao T, Yang N, Yu Y, Cui Y, Gao Y and Liu W 2023 Double Perovskite La_2MnNiO_6 as a High-Performance Anode for Lithium-Ion Batteries *Adv. Sci.* **10** 2300506
[10] Haque A, Ghosh D, Dutta U, Shukla A, Gayen A, Mahata P, Kundu A K and Motin Seikh M 2020 Change in magnetic properties of La_2MnCoO_6 in composite with $CaCu_3Ti_4O_{12}$ *J. Magn. Magn. Mater.* **494** 165847
[11] Ahmed J, Alhokbany N, Ubaidullah M, Mutehri S, Khan M A M and Alshehri S M 2020 Synthesis of double perovskite La_2MnNiO_6 nanoparticles as highly efficient oxygen evolution electro-catalysts *Ceram. Int.* **46** 20038–44
[12] Balli M, Fournier P, Jandl S and Gospodinov M M 2014 A study of the phase transition and magnetocaloric effect in multiferroic La_2MnNiO_6 single crystals *J. Appl. Phys.* **115** 173904
[13] Balli M, Fournier P, Jandl S, Truong K D and Gospodinov M M 2014 Analysis of the phase transition and magneto-thermal properties in La_2CoMnO_6 single crystals *J. Appl. Phys.* **116** 073907
[14] Barón-González A J, Frontera C, García-Muñoz J L, Rivas-Murias B, Blasco J, García-Mũoz J L, Rivas-Murias B and Blasco J 2011 Effect of cation disorder on structural, magnetic and dielectric properties of La_2MnCoO_6 double perovskite *J. Phys. Condens. Matter* **23** 496003
[15] Qian Y, Wu H, Kan E, Lu J, Lu R, Liu Y, Tan W, Xiao C and Deng K 2013 Biaxial strain effect on the electronic and magnetic phase transitions in double perovskite La_2FeMnO_6: a first-principles study *J. Appl. Phys.* **114** 063713
[16] Yoshimatsu K, Nogami K, Watarai K, Horiba K, Kumigashira H, Sakata O, Oshima T and Ohtomo A 2015 Synthesis and magnetic properties of double-perovskite oxide La_2MnFeO_6 thin films *Phys. Rev. B* **91** 054421
[17] Barrozo P, Moreno N O and Aguiar J A 2014 Ferromagnetic cluster on La_2FeMnO_6 *Adv. Mat. Res.* **975** 122–7
[18] Pezhumkattil Palakkal J, Lekshmi P N, Thomas S, Suresh K G and Varma M R 2015 Observation of high-temperature magnetic transition and existence of ferromagnetic short-range correlations above transition in double perovskite La_2FeMnO_6 *RSC Adv.* **5** 105531–10536
[19] Li Q, Xing L and Xu M 2017 Magnetic properties, resistivity and magnetoresistance effects of double perovskite $La_2Co_{1-x}Fe_xMnO_6$ *J. Alloys Compd.* **710** 771–7
[20] Gauvin-Ndiaye C, Tremblay A M S and Nourafkan R 2019 Electronic and magnetic properties of the double perovskites La_2MnRuO_6 and $LaAMnFeO_6$ (A = Ba, Sr, Ca) and their potential for magnetic refrigeration *Phys. Rev.* B **99** 125110
[21] Brahiti N, Abbasi Eskandari M, Balli M, Gauvin-Ndiaye C, Nourafkan R, Tremblay A M S and Fournier P 2020 Analysis of the magnetic and magnetocaloric properties of $ALaFeMnO_6$ (A = Sr, Ba, and Ca) double perovskites *J. Appl. Phys.* **127** 113905
[22] Aksenov V L *et al* 1999 DN-12 time-of-flight high-pressure neutron spectrometer for investigation of microsamples *Physica B* **265** 258–62
[23] Nasir Khan M, Shaheen R and Bashir J 2008 Neutron, synchrotron x-ray diffraction and x-ray absorption studies of $CaLaFeMnO_6$ double perovskite *Solid State Sci.* **10** 1634–9
[24] Kozlenko D P *et al* 2022 High pressure enhanced magnetic ordering and magnetostructural coupling in the geometrically frustrated spinel Mn_3O_4 *Phys. Rev. B* **105** 094430
[25] Mandal P, Bhat S S, Sundarayya Y, Sundaresan A, Rao C N R, Caignaert V, Raveau B and Suard E 2012 Structure and complex magnetic behavior of disordered perovskite $(Bi_{0.5}Sr_{0.5})(Fe_{0.5}Mn_{0.5})O_3$ *RSC Adv.* **2** 292–7

[26] Pal A, Singh P, Gangwar V K, Joshi A G, Khuntia P, Dwivedi G D, Gupta P K, Alam M, Anand K and Sethupathi K 2020 Probing the Griffiths like phase, unconventional dual glassy states, giant exchange bias effects and its correlation with its electronic structure in $Pr_{2-x}Sr_xCoMnO_6$ *J. Phys. Condens. Matter* **32** 215801
[27] Das R *et al* 2021 Unraveling the nature of Fe-doping mediated inter- and intra-chain interactions in $Ca_3Co_2O_6$ *J. Alloys Compd.* **851** 156897
[28] Dang N T *et al* 2019 Structural, magnetic and electronic properties of Ti-doped $BaFeO_{3-\delta}$ exhibiting colossal dielectric permittivity *J. Alloys Compd.* **808** 151760
[29] Nasir M, Khan M, Agbo S A, Bhatt S, Kumar S and Sen S 2020 Evidence of cluster-glass and Griffiths-like phases in partially ordered La_2FeMnO_6 double perovskite *J. Phys. D: Appl. Phys.* **53** 375003
[30] Borges R P, Ott F, Thomas R M, Skumryev V, Coey J M D, Arnaudas J I and Ranno L 1999 Field-induced transition in the paramagnetic state of $(Sm_{0.65}Sr_{0.35})MnO_3$ associated with magnetic clusters *Phys. Rev.* B **60** 12847–51
[31] Hosaka Y, Ichikawa N, Saito T, Manuel P, Khalyavin D, Attfield J P and Shimakawa Y 2015 Two-dimensional charge disproportionation of the unusual high valence state Fe^{4+} in a layered double perovskite *J. Am. Chem. Soc.* **137** 7468–73
[32] Zhou X-D, Cai Q, Yang J, Kim M, Yelon W B, James W J, Shin Y-W, Scarfino B J and Anderson H U 2005 Coupled electrical and magnetic properties in $(La,Sr)FeO_{3-\delta}$ *J. Appl. Phys.* **97** 9710C314
[33] Tong W, Zhang B, Tan S and Zhang Y 2004 Probability of double exchange between Mn and Fe in $LaMn_{1-x}Fe_xO_3$ *Phys. Rev.* B **70** 014422
[34] Shahee A, Singh K, Choudhary R J and Lalla N P 2015 Evidence of ferromagnetic short-range correlations in cubic $La_{1-x}Sr_xMnO_{3-\delta}$ ($x = 0.80, 0.85$) above antiferromagnetic ordering *physica status solidi (b)* **252** 1832–8
[35] Islam M A, Tarek M, Asif Adib M and Basith M A 2024 B-site disorder driven Griffiths-like phase and electrochemical behavior in Y_2NiCrO_6 double perovskite *J. Phys. D: Appl. Phys.* **57** 215302
[36] Silva R S, Santos C, Escote M T, Costa B F O, Moreno N O, Paz S P A, Angélica R S and Ferreira N S 2022 Griffiths-like phase, large magnetocaloric effect, and unconventional critical behavior in the $NdSrCoFeO_6$ disordered double perovskite *Phys. Rev.* B **106** 134439
[37] Silva A G, Salcedo Rodrıguez K L, Contreras Medrano C P, Lourenco G S G, Boldrin M, Saitovitch E B and Bufaiçal L 2021 Griffiths phase and spontaneous exchange bias in $La_{1.5}Sr_{0.5}CoMn_{0.5}Fe_{0.5}O_6$ *J. Phys. Condens. Matter* **33** 065804
[38] Das M, Sarkar P and Mandal P 2020 Non-Griffiths-like cluster formation in the double-perovskite Gd_2CoMnO_6: evidence from critical behavior *Phys. Rev.* B **101** 144433
[39] Kozlenko D P *et al* 2021 Competing magnetic states in multiferroic $BaYFeO_4$: a high magnetic field study *Phys. Rev. Mater.* **5** 044407
[40] Wareppam B, Kuzmann E, Garg V K and Singh L H 2023 Mössbauer spectroscopic investigations on iron oxides and modified nanostructures: a review *J. Mater. Res.* **38** 937–57
[41] Huo G, Song D, Yang Q and Dong F 2008 Structure, magnetic and electrical transport properties of the perovskites $Sm_{1-x}Ca_xFe_{1-x}Mn_xO_3$ *Ceram. Int.* **34** 497–503
[42] Narsinga Rao G, Chen J W, Neeleshwar S, Chen Y Y and Wu M K 2009 Enhanced magnetoresistance and Griffiths phase induced by Mo substitution in $La_{0.7}Ca_{0.15}Sr_{0.15}Mn_{1-x}Mo_xO_3$ ($0 \leqslant x \leqslant 0.05$) *J. Phys. D: Appl. Phys.* **42** 095003
[43] Fita I, Troyanchuk I O, Zajarniuk T, Iwanowski P, Wisniewski A and Puzniak R 2018 Exchange bias effect and Griffiths phase coexistence in the disordered cobaltite $Gd_{0.5}Sr_{0.5}CoO_{3-\delta}$ *Phys. Rev.* B **98** 214445